

## Using $\gamma$ rays to disentangle fusion-fission and quasifission near the Coulomb barrier: A test of principle in the fusion-fission and quasielastic channels

E. Vardaci<sup>1,2,\*</sup>, A. Pulcini<sup>1,2,†</sup>, E. M. Kozulin<sup>3</sup>, I. Matea<sup>4</sup>, D. Verney<sup>4</sup>, A. Maj<sup>5</sup>, C. Schmitt<sup>6</sup>, I. M. Itkis<sup>3</sup>, G. N. Knyazheva<sup>3</sup>, K. Novikov<sup>3</sup>, N. Kozulina<sup>3</sup>, I. M. Harca<sup>3</sup>, I. V. Kolesov<sup>3</sup>, K. Saveleva<sup>3</sup>, V. V. Kirakosyan<sup>3</sup>, O. Dorvaux<sup>7</sup>, M. Ciemala<sup>5</sup>, S. Brambilla<sup>8</sup>, M. Ashaduzzaman<sup>1,2,9</sup>, B. De Canditiis<sup>1,2</sup>, A. Di Nitto<sup>1,2</sup>, D. Quero<sup>1,2</sup>, C. Parascandolo<sup>2</sup>, D. Pierroutsakou<sup>2</sup>, P. K. Rath<sup>1,2,10</sup>, G. Sposito<sup>1,2</sup>, G. La Rana<sup>1,2</sup>, A. Bracco<sup>8,11</sup>, F. Camera<sup>8,11</sup>, O. Stezowski<sup>8,11</sup>, C. Borcea<sup>12</sup>, S. Calinescu<sup>12</sup>, C. Petrone<sup>12</sup> and J. Wilson<sup>4</sup>

<sup>1</sup>*Dipartimento di Fisica "E. Pancini", Università degli Studi di Napoli "Federico II", 80126 Napoli, Italy*

<sup>2</sup>*Istituto Nazionale di Fisica Nucleare, Sezione di Napoli, 80126 Napoli, Italy*

<sup>3</sup>*Flerov Laboratory of Nuclear Reaction, Joint Institute for Nuclear Research, 141980 Dubna, Moscow region, Russia*

<sup>4</sup>*IPN, CNRS/IN2P3, Université Paris-Saclay, 91405 Orsay, France*

<sup>5</sup>*Institute of Nuclear Physics PAN, Krakow, Poland*

<sup>6</sup>*IPHC, 67037 Strasbourg, France*

<sup>7</sup>*IPHC, CNRS/IN2P3, Université de Strasbourg, 67037 Strasbourg, France*

<sup>8</sup>*Istituto Nazionale di Fisica Nucleare, Sezione di Milano, Milano, Italy*

<sup>9</sup>*Department of Electrical and Electronic Engineering, Green University of Bangladesh, Dhaka, Bangladesh*

<sup>10</sup>*Centurion University, Paralakhemundi, 761211 Odisha, India*

<sup>11</sup>*Università degli Studi di Milano, Milano, Italy*

<sup>12</sup>*Horia Hulubei National Institute for Research and Development in Physics and Nuclear Engineering (IFIN-HH), Bucharest, Magurele, Romania*



(Received 9 March 2020; accepted 27 April 2020; published 15 June 2020)

The overlap in the mass symmetric region of the reaction products from fusion-fission and quasifission complicates the assignment of symmetric events to complete fusion on the basis of the mass distribution alone. Additional observables, besides mass distribution, should be used. The approach proposed here relies on the fact that fusion-fission and quasifission are characterized by different timescales. Within this framework, we performed a detailed study to find out how timescales can be probed via angular momentum transfer as measured via  $\gamma$ -ray multiplicities. The proof of principle was carried out by measuring the  $\gamma$  rays in coincidence with fusion-fission and quasielastic binary fragments in the reaction  $^{32}\text{S} + ^{197}\text{Au}$  at beam energy near the Coulomb barrier. The experiment was performed at the Accélérateur Linéaire Tandem à Orsay (ALTO) facility at the Institut De Physique Nucléaire (IPN) in Orsay (France) using a detection setup consisting of ORGAM (Orsay GAMMA) and PARIS (Photon Array Radioactive Ion Stable beams)  $\gamma$ -detectors arrays coupled with the CORSET (CORrelation SETup) time-of-flight spectrometer. Results of the sensitivity of this method to distinguish reaction channels with different dynamics are discussed.

DOI: [10.1103/PhysRevC.101.064612](https://doi.org/10.1103/PhysRevC.101.064612)

### I. INTRODUCTION

Heavy-ion-induced fusion reactions at bombarding energies around the Coulomb barrier have been very successfully used for the production of superheavy elements (SHE) [1–6]. To select the optimal reactions for the production of new elements heavier than Og and/or new isotopes around the superheavy island of stability, the measurement of fusion cross sections is an essential step [7]. In fusion events, a compound nucleus (CN) may evolve toward fission (fusion-fission, FF) or become an evaporation residue (fusion-evaporation, ER) after the evaporation of light particles. The fusion cross section is measured by summing the cross sections of these two

decay channels. In reactions involving medium-mass nuclei, the fission and evaporation cross sections can be of about the same magnitudes [8,9]. This particular condition constitutes an advantage in the study of fission dynamics of medium-mass nuclei [10,11].

In the case of reactions between massive nuclei necessary for the search of superheavy elements, the evaporation residue's cross section is negligible with respect to that of the fission. Therefore, it is sufficient to select and count the fission events to estimate the fusion cross section [12]. Fission events are selected by detecting in coincidence fragments produced in binary reactions. However, at energies around the Coulomb barrier, the quasifission (QF) reaction mechanism, which also gives rise to binary products, becomes dominant and counteracts the complete fusion [12]. Furthermore, the mass distribution of binary products of QF reactions, due to the high production yield, can dominate the fragment's

\*Corresponding author: vardaci@na.infn.it

†Corresponding author: pulcini@na.infn.it

symmetric-mass region, where also FF events are expected. Consequently, in the case of reactions between massive nuclei, the estimate of fusion cross sections, based on counting symmetric or nearly symmetric mass split events, can be biased because of the overlap of QF and FF binary events. Even if in the asymmetric region of the mass distribution it is possible to disentangle, to some extent, the components of QF and asymmetric FF modes, this is not possible in the symmetric-mass region where the two processes are overlapped. Therefore, the overlap of QF and FF events constitutes an inescapable problem when CN cross sections have to be estimated [13].

Within the present work, we investigate if additional observables can be employed to unambiguously separate the FF and QF products, at least to some extent. In our view, these additional observables should reflect the differences between the slower dynamical evolution of the system passing through an equilibrium stage giving rise to the FF products, and the faster QF mechanism where the mass transfer and energy dissipation are strongly driven by shell effects [13–15]. Many experimental and theoretical works aimed at estimating the timescale of FF and QF confirm that QF takes place on a timescale of  $\lesssim 10^{-20}$  s, whereas FF typically occurs on longer timescales, from  $\approx 10^{-19}$  to  $\approx 10^{-16}$  s [16–23].

It has been demonstrated by series of works [24–31] that precission light particles can provide the timescale of the dynamical evolution of the compound nucleus from its formation up to the scission in two fragments. However, their emission probability is negligible in the typical reactions used for the SHE production in the FF and QF channels. A possible difference among the QF and FF paths can be found in the angular momentum dissipated during the dynamical evolution of the composite intermediate system, up to the reseparation stage, where the fragment production occurs. The entrance channel orbital angular momentum is fully transferred into internal degrees of freedom of the compound nucleus in FF, whereas only a fraction of it is available for the QF products, being the QF process faster [32–34]. It is reasonable to suspect that the fragments of FF may reach a higher spin than those produced by QF. Consequently, the  $\gamma$ -ray multiplicity distributions  $M_\gamma$ , namely, the distribution of the number of  $\gamma$ -rays emitted per event, should reach higher average values in the case of FF events.

Independent information about low and high angular momentum transfer paths (respectively, QF and FF channels) can be extracted from discrete  $\gamma$  transitions as well as from the  $\gamma$ -ray multiplicity in binary events. Hence, by measuring the  $\gamma$  rays in coincidence with binary fragments, a disentanglement of QF and FF might be attained. Therefore, the observable we focus on here are the  $\gamma$  rays and their multiplicity  $M_\gamma$  in the binary channels.

In order to test this method, namely the separation of a faster process from a slower one by  $\gamma$ -ray multiplicity, the reaction  $^{32}\text{S} + ^{197}\text{Au}$ , at the bombarding energy  $E_{\text{LAB}} = 166$  MeV, near the Coulomb barrier  $V_{\text{Coul}}$  ( $E_{\text{c.m.}}/V_{\text{Coul}} = 1.01$ ), was carried out at the Tandem Accélérateur Linéaire Tandem à Orsay (ALTO) accelerator facility at Institut De Physique Nucléaire (IPN) Orsay (France).  $E_{\text{c.m.}}$  is the energy available in the center of mass frame. This reaction is characterized by a large FF cross section and a negligible QF cross section

[35,36]. At the same time, this reaction has a dominant contribution from the quasielastic (QE) channel, which is governed by transfers of few nucleons and relatively small energy and angular momentum dissipation [37,38]. The FF and QE channels can be well separated by exploiting the large differences in the mass and total kinetic energy (TKE) distributions. Binary products of QE reactions are located in the mass region around the mass of the target and projectile nuclei and their TKE is about equal to the entrance channel relative motion energy. In FF, the mass distribution is centered around symmetric splitting and has a characteristic width [39]. The TKE distribution is instead expected to follow Viola systematics [40]. Because of these important differences, this proposed reaction represents a suitable benchmark to characterize the  $\gamma$ -ray multiplicities dependence on reaction timescales by using the measurements of  $\gamma$  rays in coincidence with the binary fragments assigned to the QE and FF, i.e., from the faster and slower processes, respectively.

If the hypothesis that a higher angular momentum population corresponds to a larger interaction time is valid, the  $\gamma$  transitions measured in coincidence with the QE component should come from nuclei populated to lower angular momentum regions and the  $\gamma$  multiplicity should be smaller than the one in coincidence with the fragments in the symmetric mass region. This would prove the concept and would open the road to experiments to distinguish between QF and FF in the symmetric region by employing an additional probe.

After a brief description of the experimental setup, the result of this approach will be discussed.

## II. EXPERIMENTAL SETUP

A 350- $\mu\text{g}/\text{cm}^2$ -thick self-supporting  $^{197}\text{Au}$  target was bombarded with a  $^{32}\text{S}$  beam at  $E_{\text{LAB}} = 166$  MeV. The center of mass energy  $E_{\text{c.m.}}$  is such that  $E_{\text{c.m.}}/V_{\text{Coul}} = 1.01$ . The Tandem accelerator provided, on average, a continuous beam of intensity of 70 nA during the 2-day-long measurement.

Fragments from binary reactions were detected in coincidence by the two-arm TOF spectrometer CORSET (CORrelation SETup) [41]. Each arm consists of a microchannel plate (MCP) and a position-sensitive MCP acting as start and stop detectors, respectively. The arms were placed at  $68^\circ$  and  $-66.5^\circ$  with respect to the beam axis to maximize symmetric fragment detection. Each start detector covers an area of  $20 \times 30$  mm<sup>2</sup> and was placed at 6 cm from the target. Each position-sensitive stop detector covers an area of  $60 \times 40$  mm<sup>2</sup> and was mounted 21 cm away from the start detector. In the event-by-event offline analysis, the positions and time of flights of the fragments are translated into fragment mass numbers  $A_{1,2}$ , velocity vectors  $\vec{v}_1$ ,  $\vec{v}_2$ , and TKE by employing standard two-body conservation laws [41]. With a time-of-flight resolution of 150 ps and an angular resolution of  $0.3^\circ$ , the masses  $A_{1,2}$  of the two products in coincidence were determined with a resolution better than 3 amu (FWHM) and energy resolution of 5 MeV. In this procedure, energy losses of the fragments in different passive absorbers (the target and the foils of the CORSET start detectors) are accounted for.

The prompt  $\gamma$  rays were detected with ORGAM (ORSay GAMma) [42], an array of high-resolution Ge detectors, individually surrounded by BGO anti-Compton shields, and

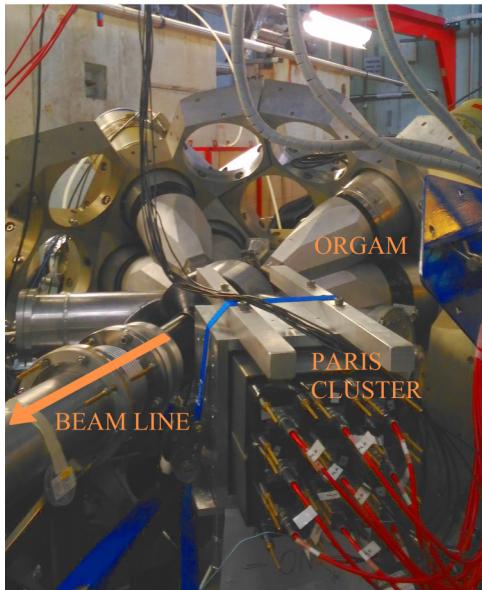
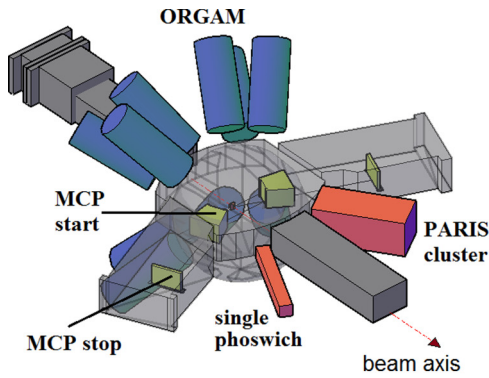


FIG. 1. A schematic drawing and a photo of the experimental setup used in the experiment. Reprinted figure from the work of Kozulin *et al.* [36] with kind permission from *The European Physical Journal A (EPJA)*.

PARIS (Photon Array Radioactive Ion Stable beams) [43], an array of high-efficiency  $\text{LaBr}_3(\text{Ce})\text{-NaI}(\text{Tl})$  phoswiches. For this experiment, 10 ORGAM detector units were used, all placed at backward angles at 18 cm from the target center, and 10 PARIS units, 9 of them closely packed together at 38 cm from the target center plus a single unit placed at 30 cm from the target center. All PARIS phoswiches were mounted at forward angles. A schematic drawing and a photo of the experimental setup are shown in Fig. 1.

The energy calibration of each  $\gamma$ -ray detector was performed using several standard radioactive sources ( $^{60}\text{Co}$ ,  $^{137}\text{Cs}$ ,  $^{152}\text{Eu}$ , and  $^{241}\text{Am-}^9\text{Be}$ ). It should be noted that the last calibration point used in the energy calibration of the PARIS detectors was at  $E_\gamma = 4.4$  MeV. Therefore, the high-energy calibration of PARIS was extrapolated from the low-energy one. The measured photopeak efficiencies in the low-energy range were 1.5% and 0.7% for ORGAM and PARIS, respectively. ORGAM has a better energy resolution (4 keV at 1408 keV) than PARIS (60 keV at 1332 keV);

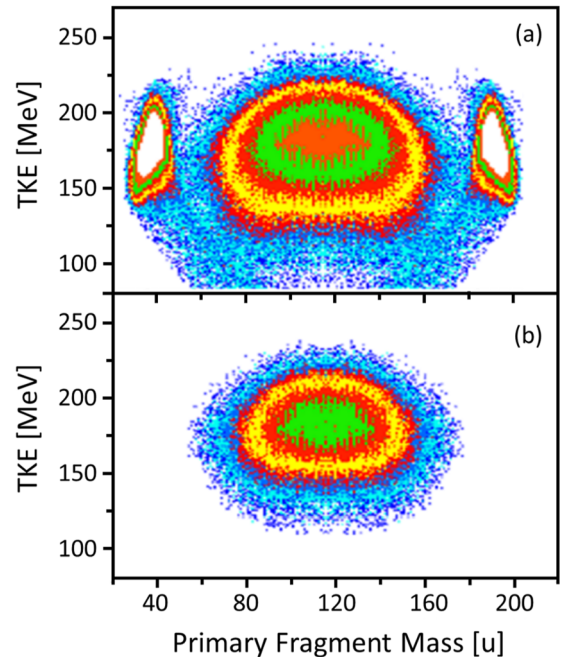


FIG. 2. (a) Mass-TKE matrix of the binary events from the reaction  $^{32}\text{S}$  ( $E_{\text{lab}} = 166$  MeV) +  $^{197}\text{Au}$  without conditions and (b) applying the full momentum transfer condition and gate on FF only.

however, PARIS provides additional information by spanning a larger dynamical range (up to 20 MeV), compared to ORGAM (up to 2.4 MeV).

The readout of the PARIS detectors was accomplished with the newly designed LaBrPRO module [44]. The energy and time signals of the three setups CORSET + ORGAM + PARIS were fed into the VIPERS data acquisition system [45–49] running a VME front-end with commercial TDC and ADC modules.

Binary fragments and  $\gamma$  rays were detected in singles and in prompt coincidence. The  $\gamma$ -ray multiplicity  $M_\gamma$  in coincidence with QE and FF fragments were determined from the number of  $\gamma$  detectors hit in the binary event (QE or FF), the so-called  $\gamma$ -fold. The fold-to- $M_\gamma$  conversion was performed as it will be shown in the next sections.

### III. SELECTION OF BINARY REACTION CHANNELS

If complete fusion occurs, the reaction  $^{32}\text{S}$  ( $E_{\text{lab}} = 166$  MeV) +  $^{197}\text{Au}$  leads to the neutron-deficient  $^{229}\text{Am}$  compound nucleus, excited at  $E_{\text{CN}}^* \approx 43$  MeV. The ultimate goal of the experiment is to study the trend of  $M_\gamma$  when  $\gamma$ -ray events are gated on FF and QE events separately. In this study, we widely profit from the measurements of mass and TKE of the coincident fragments and the fact that FF and QE events are well separated in the mass-TKE correlation matrix.

Figure 2(a) shows the binary fragment mass-TKE matrix obtained in this experiment for center-of-mass angles at  $(90 \pm 10)^\circ$ . The mass-TKE matrix for binary events is reconstructed from CORSET coincidence data alone. The measurements of the event-by-event time of flight and the flight path of each

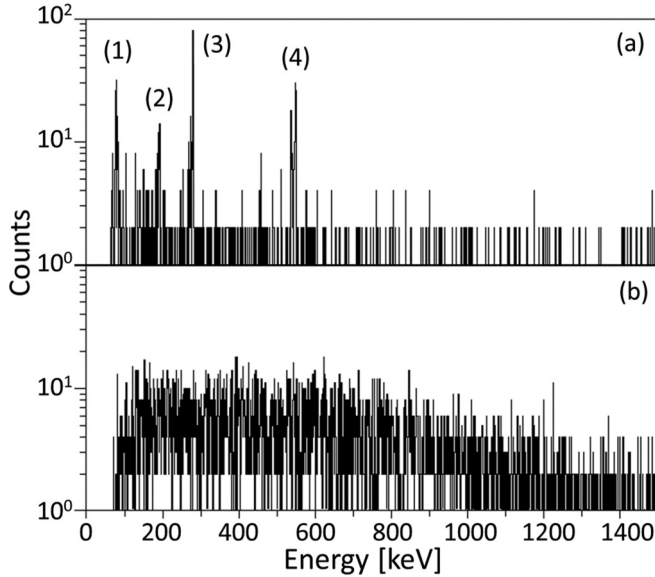


FIG. 3. (a)  $\gamma$ -ray energy spectra detected in coincidence with QE events. Marked peaks are  $^{197}\text{Au}$  transitions. Energies of the peaks are, in order from (1) to (4),  $77 \pm 2$ ,  $192 \pm 3$ ,  $280 \pm 2$ , and  $549 \pm 4$  keV. Candidates  $^{197}\text{Au}$   $\gamma$  transitions are 77.351, 191.437, 279.01, and 547.5 keV. (b)  $\gamma$ -ray energy spectra detected in coincidence with FF events.

fragment in binary coincidence are used to reconstruct the event-by-event velocity vectors  $\vec{v}_1$ ,  $\vec{v}_2$  of the two emerging fragments; then, from the two velocity vectors, by considering mass and momentum conservation laws, masses and energies of each couple of fragments are reconstructed. Velocity vectors are needed to obtain the mass distribution as well as to correct the  $\gamma$ -energy spectra for Doppler effect.

By considering only the full momentum transfer (FMT) and the  $|\vec{v}_2|$  versus  $|\vec{v}_1|$  event matrix, it is possible to isolate the FF reaction products. The FMT selection is obtained by requiring that the sum of velocity vector projections on the reaction plane is equal to the center-of-mass velocity (see Ref. [50] for more details). Thus, the mass-TKE distribution in Fig. 2(b), obtained requiring the FMT and selection of FF events in the velocity matrix  $|\vec{v}_2|$  versus  $|\vec{v}_1|$ , can be considered to originate in FF reactions being the QF component negligible. The two loci on the left and right of the FF region [Fig. 2(a)] can be ascribed to the QE events.

#### IV. SELECTION OF $\gamma$ RAYS IN COINCIDENCE WITH BINARY REACTION CHANNELS

By gating on specific regions of the mass-TKE matrix, one is able to select only  $\gamma$  rays associated to each reaction mechanisms, FF or QE. To extract  $\gamma$ -energy spectra, however,  $\gamma$ -ray events have to be properly processed. For instance, for both PARIS and ORGAM, gates have been considered on time signals to isolate the prompt  $\gamma$ -ray component of the energy spectra. The anticoincidence condition between Ge and BGO detectors suppresses the Compton component of the ORGAM energy spectrum. An example of such spectra resulting from this procedure is shown in Fig. 3. Both spectra

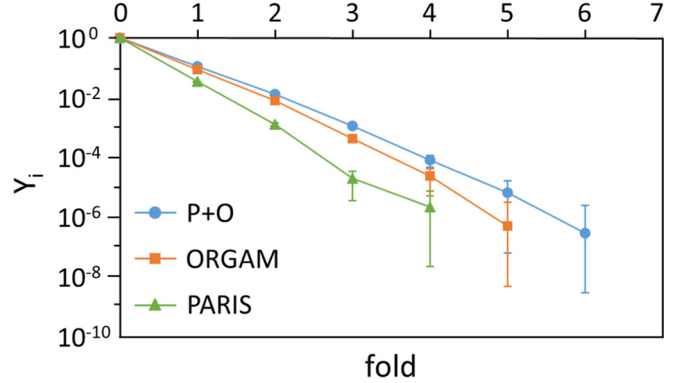


FIG. 4.  $\gamma$ -fold distributions for  $\gamma$  rays obtained with PARIS alone (triangles, green full line), ORGAM alone (squares, red full line), and PARIS and ORGAM considered as a single array (labeled as P + O, circles blue full line) in coincidence with all binary events. Lines are drawn to guide the eyes. Counts are normalized to the total number of binary coincidence events. The average folds are  $0.12 \pm 0.04$  (P + O),  $0.03 \pm 0.02$  (PARIS), and  $0.09 \pm 0.03$  (ORGAM).

correspond to a single ORGAM detector. In Fig. 3(a),  $\gamma$  rays are in coincidence with QE events; in Fig. 3(b)  $\gamma$  rays are in coincidence with FF events. The most visible peaks of the QE  $\gamma$  spectrum can be assigned to the low energy and low angular momentum  $^{197}\text{Au}$  transitions (marked with numbers from 1 to 4) and are strongly suppressed in the spectrum in coincidence with FF events.

By taking advantage of the unambiguously assignment of QE and FF events in the mass-TKE matrix, it is possible the extraction of the QE and FF  $\gamma$ -fold distribution, namely, the distribution of the number of  $\gamma$  rays detected per event, by gating on identified events in the mass-TKE distribution only. In addition to the previous processing of  $\gamma$  rays, the fold extracted from PARIS detectors had to be corrected for cross talk among the phoswiches packed in a  $3 \times 3$  cluster configuration. The correction has been done using a simple algorithm: If two or more neighboring detectors produce signals in a single event, their total contribution to the fold is considered to be 1. Background has been also subtracted. An estimate of background gives 1.5% for ORGAM and 0.5% for PARIS.

#### V. THE $\gamma$ -RAY FOLD DISTRIBUTIONS

Figure 4 shows the comparison between the  $\gamma$ -fold distributions obtained with PARIS alone (triangles, green full line), ORGAM alone (squares, red full line), and PARIS + ORGAM considered as a single array (labeled as P + O, circles, blue full line) in coincidence with all binary events. For each distribution, the yields  $Y_i$  are normalized to the yield of binary events without  $\gamma$  rays in coincidence (fold = 0). The index  $i$  denotes the PARIS, ORGAM, and PARIS + ORGAM arrays. At this first step, no efficiency correction is performed on these data.

Average fold values are  $0.03 \pm 0.02$  for PARIS alone,  $0.09 \pm 0.03$  for ORGAM alone, and  $0.12 \pm 0.04$  for PARIS + ORGAM (P + O). These average values are

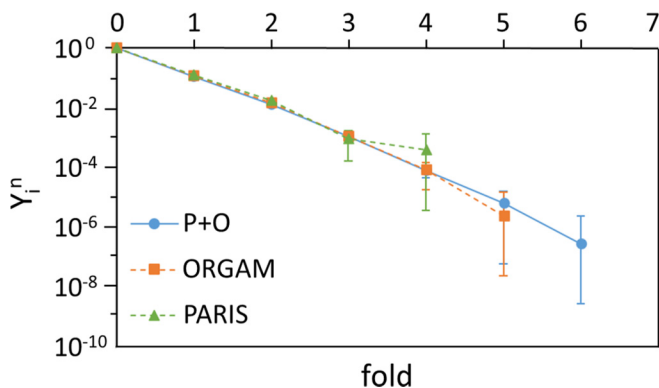


FIG. 5.  $\gamma$ -fold distributions for  $\gamma$  rays detected in coincidence with binary events by ORGAM and PARIS together (P + O, circles, blue solid line) compared to PARIS and ORGAM distributions, renormalized for total efficiency (ORGAM, squares, red dashed line, and PARIS, triangles, green dashed line). The average folds are  $0.12 \pm 0.04$  (P + O),  $0.13 \pm 0.06$  (PARIS), and  $0.13 \pm 0.04$  (ORGAM).

consistent with the different efficiencies between PARIS and ORGAM. Even though the intrinsic efficiency of a single PARIS unit is larger than the one of an ORGAM unit, due to the different geometrical configuration, the total efficiency of the 10 used ORGAM units is larger than the total efficiency of the 10 PARIS units used. The lower average fold of the PARIS array is the straightforward consequence of the smaller total efficiency.

To verify that the differences between the three distributions are a direct consequence of the different efficiencies, the fold distributions have been normalized to the efficiency ratios. The energy averaged efficiencies are  $\varepsilon_P = 0.6\%$ ,  $\varepsilon_O = 1.3\%$ , and  $\varepsilon_{P+O} = \varepsilon_P + \varepsilon_O = 1.9\%$  for PARIS, ORGAM, and PARIS + ORGAM, respectively. The PARIS and ORGAM distributions have been normalized to the P + O one. The normalization factors depend on the efficiency ratios and fold according to the ansatz  $(\varepsilon_{P+O}/\varepsilon_i)^{\text{fold}}$ , where the index  $i$  denotes the PARIS and ORGAM arrays. The distributions are shown in Fig. 5. The average fold values are now  $0.13 \pm 0.06$  for PARIS,  $0.13 \pm 0.04$  for ORGAM, and  $0.12 \pm 0.04$  for P + O. The excellent agreement between the average fold values and the shapes of the three fold distributions confirms that the differences in the raw fold distributions are due to the differences in the total efficiency. On the basis of the results above, in the following the data analysis will refer only to the PARIS + ORGAM fold distribution.

Finally, the fold distributions of  $\gamma$  rays detected in coincidence with FF and QE products were extracted and are compared in Fig. 6. The QE  $\gamma$ -fold distribution drops much more quickly than the FF one, by orders of magnitude. Furthermore, in FF events, up to six  $\gamma$  rays have been detected in coincidence, whereas in QE events the maximum fold is 2.

If we now assume that the  $\gamma$ -ray energy-averaged detection efficiency does not change sensibly with the binary channel (QE or FF) (the  $\gamma$  ray energies span the same energy range in QE and FF; see Fig. 3), these data indicate that the  $\gamma$ -fold distribution is an observable sensitive to the reaction timescale. The expected lower amount of orbital angular

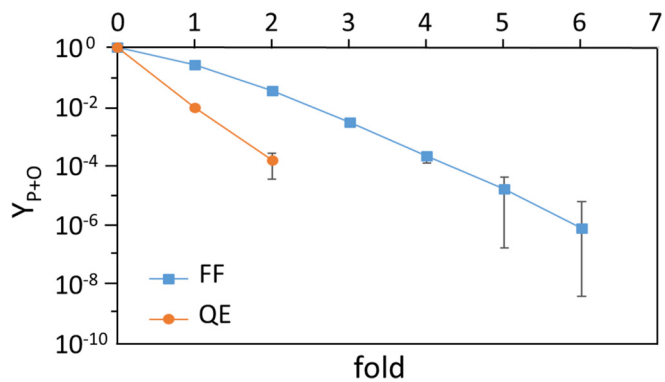


FIG. 6.  $\gamma$ -fold distributions detected with PARIS + ORGAM (P + O) in coincidence with QE and FF products. The average folds are  $0.26 \pm 0.07$  (FF) and  $0.009 \pm 0.004$  (QE).

momentum transferred during the faster process explains the smaller average fold in the QE channel.

## VI. THE $\gamma$ -RAY FOLD DISTRIBUTION AND THE RESPONSE MATRIX OF ORGAM + PARIS

The conversion of the fold distribution into  $\gamma$ -multiplicity distribution is usually a complex task, which requires a well-constrained guess. The complexity is due to the fact that the detected number of  $\gamma$ 's in each event is less than the number of  $\gamma$ 's truly emitted in an event because of the limited (intrinsic and geometrical) efficiency of the  $\gamma$  detectors. For instance, fold = 1 events means that only one  $\gamma$  ray is detected out of the many (unknown number) emitted. Therefore, fold = 1 events are the overlap of a distribution of events associated with the emission of an unknown number of  $\gamma$  rays, being the process of detection of stochastic origin. In other words, it is necessary to calculate what is the probability that fold = 1, for instance, is due to a multiplicity of 1, 2, 3, ...,  $n$   $\gamma$  rays emitted. This probability represents the so-called response function of the detection system. In general, we expect that with the increasing of the number of  $\gamma$ 's truly emitted in the decay process also the probability of detecting more than one  $\gamma$  ray increases. However, the rate of such increment is strongly dependent on the detector efficiency. Finally, to obtain an estimate of the multiplicity distribution, since we measure the fold distribution, the response function should be inverted. We will indeed proceed differently, as will be shown later.

To compute this response function in a way to include the features of PARIS + ORGAM setup, namely the geometrical efficiency and the dependence of the intrinsic efficiency on the energy of the  $\gamma$  rays as measured, we prepared a Monte Carlo simulation code (SiMCA). This code computes the conditional probability  $P(F, M_\gamma)$  that a number  $F$  of  $\gamma$  rays, out of  $M_\gamma$  emitted in a physical event, are detected. In other words, the code calculates the probability that a fold  $F$  comes from a multiplicity  $M_\gamma$ .

The code starts by generating  $M_\gamma$   $\gamma$  rays per event, from a user-defined distribution limited in the range  $M_{\gamma,\text{min}}$  to  $M_{\gamma,\text{max}}$ , each with a randomly generated direction and energy. With the detection probability dependent on the energy and

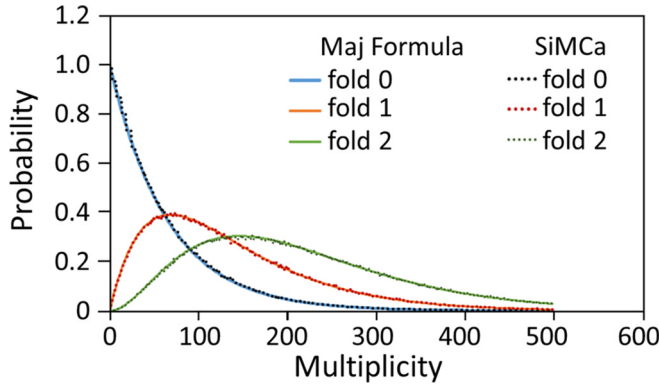


FIG. 7. Comparison between the multiplicity distribution computed with the Monte Carlo code (SiMCA, dots) and the Maj formula [51] for three different fold values. Only geometrical efficiency is considered.

spatial distribution of the  $\gamma$  rays, the code requires in input a user-defined function for the energy distribution, while the emission direction is considered isotropic. Afterward, the code determines the amount of  $\gamma$  rays that hit the detectors by taking into account the emission direction and the geometrical configuration of the detection array given by the user. For each  $\gamma$  ray firing a detector, the code compares a randomly generated number in the interval  $[0, 1]$  with the intrinsic efficiency of the fired detector. The intrinsic efficiency in the SiMCA code follows the equation  $\varepsilon(E) = A_1 e^{(-E/E_1)} + \varepsilon_1$ , in which  $A_1$ ,  $E_1$ , and  $\varepsilon_1$  are parameters obtained from the fit to experimental data on efficiency. Only if the random number is lower than the efficiency is the  $\gamma$  ray considered as detected. By the computed number  $F$  of  $\gamma$  rays detected out of  $M_\gamma$  rays generated, and by repeating the process enough times to have a sufficient precision, the probability matrix  $P(F, M_\gamma)$  is generated.

To test the validity of this method, a comparison has been made with the results of the formula proposed in Ref. [51] by Maj *et al.* for the probability  $P(F, M_\gamma)$ . This formula is based on a recursive algorithm and takes into account a total efficiency independent from the  $\gamma$ -ray energy.

A first comparison has been carried out by using in SiMCA code and in the Maj formula an intrinsic efficiency equal to 1, independent from the  $\gamma$ -ray energy; i.e., the fold has been obtained by considering only the geometrical efficiency. Figure 7 shows the probabilities to have a fold of 0, 1, and 2 as function of the  $M_\gamma$  ranging from 0 to 500. As expected, the probability to detect more than one  $\gamma$  ray increases as the multiplicity increases and the maximum of the curve for each fold moves toward larger multiplicities. The distributions obtained by the two methods are indistinguishable.

To check the effects of the  $\gamma$ -ray energy dependence of the efficiency, another comparison has been made between the two methods. In the Maj formula [51], only an average energy-independent efficiency is accounted for. For this case, we used the efficiency obtained as the average over the energy and over different detectors. In our code, we take advantage of the intrinsic flexibility of a Monte Carlo approach and we used the measured efficiency curve for each of the detectors.

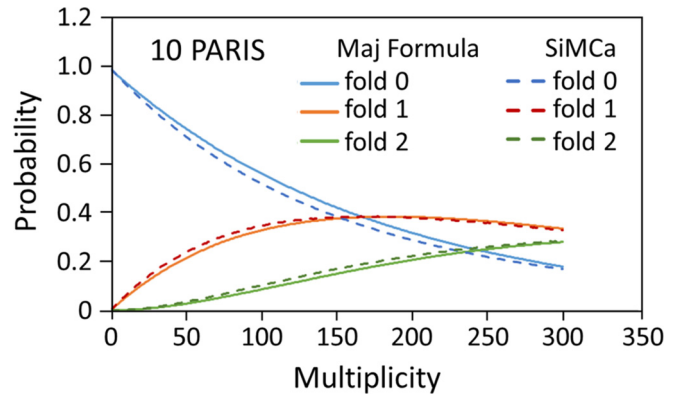


FIG. 8. Comparison between the calculation of the probability  $P(F, M_\gamma)$  made with SiMCA code, which now includes the dependence of the detection efficiency on the  $\gamma$ -ray energy and the formula in Ref. [51] for three different values of fold. Dashed lines are the predictions of the SiMCA code; solid lines are the results of the Maj formula.

This flexibility is for us very valuable because ORGAM and PARIS detectors are characterized by very different intrinsic efficiencies. This means that in a single tool we can include detectors with different performances. In order to reduce the differences with respect to the Maj's formula results, in our simulations the energy spectrum is chosen as a flat distribution between 150 and 3000 keV. Figure 8 shows the comparison between the two different methods for three different values of the fold (0, 1, and 2). There are only slight differences between the two methods, which seem to disappear for increasing fold values above 2. This is indeed a consequence of the limited angular coverage of PARIS + ORGAM. For a larger coverage of the solid angle, the differences are more marked. This behavior can be evidenced when the number of PARIS detectors is doubled or quadrupled as shown in Figs. 9(a) and 9(b), respectively. The curves for each fold have the same shape, but they are shifted by a relatively large amount. This means that the conversion fold to  $M_\gamma$  will be affected. Another remarkable feature is that the curves for fold  $> 0$  are narrower and the maxima progressively shift toward lower values of the multiplicity. Consequently, larger total efficiency translates in a smaller error in the conversion fold to  $M_\gamma$ .

Even if all the comparisons discussed so far have been performed using uniform distributions of  $M_\gamma$ , SiMCA allows us to use any kind of multiplicity distribution function. Essentially, we have developed a code able to simulate the fold distribution for a given multiplicity distribution by taking into account the geometrical and the intrinsic efficiency of all the elements constituting the detection setup. However, we need to invert the process, namely, to find the  $M_\gamma$  distribution for a given or measured  $\gamma$ -fold distribution. This inversion is not straightforward and can be source of errors. Therefore, it is more convenient to assume a realistic multiplicity distribution and compare the resulting fold distribution (filtered via the response function) with the measured one. For these reasons, a search for a multiplicity distribution, grounded on some physical information, was carried out.

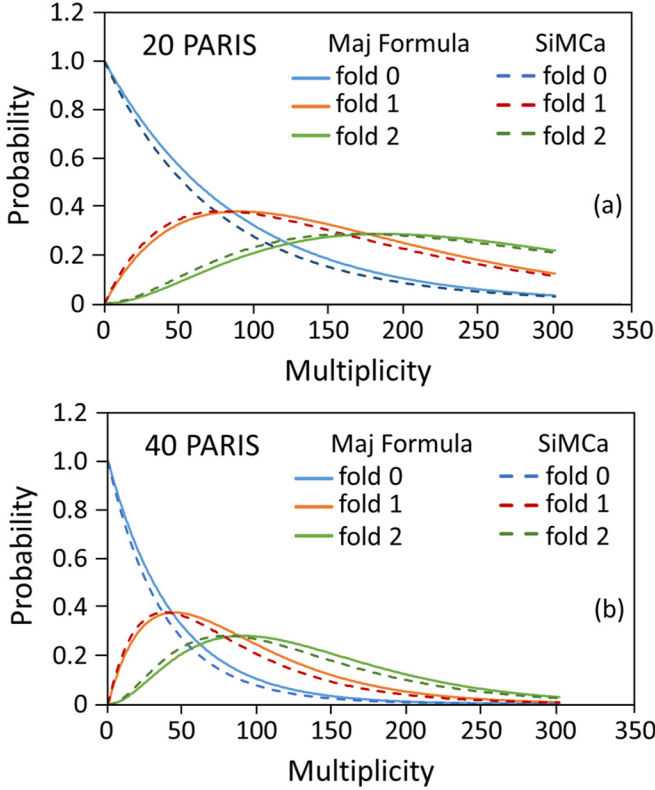


FIG. 9. Same as in Fig. 8 but with doubled (a) and quadrupled (b) PARIS efficiency.

## VII. FROM $\gamma$ -RAY FOLD DISTRIBUTION TO MULTIPLICITY DISTRIBUTION

In order to define the best guess for the true multiplicity distribution, we started from the well-known method proposed by Ockels [52]. This method provides a rapidly converging algorithm to compute the first few moments of the multiplicity distribution for a given measured fold distribution and efficiency of the  $\gamma$ -ray detecting array. The method is particularly suited in cases where a low fold ( $\leq 4$ ) is available. In general, the larger is the fold measured, the larger is the number of moments that can be computed. The method also provides a mean to compute errors on these shape parameters. Consistently, the error becomes bigger by increasing the order of the moment. By applying this method (Eq. (16) in Ref. [52]) to the FF and QE fold distributions in Fig. 6, we can determine some moments of the corresponding multiplicity distributions. Afterward, by fixing the moments, we can choose from among several trial distributions, with moments fixed as computed, the one that best reproduces, once being filtered by the response function, the measured fold distributions. With this ansatz, we obtain the experimental multiplicity distributions.

By using Eq. (16) in Ref. [52], we were able to compute the first three moments of the experimental multiplicity distributions of the FF and QE channels. The values are shown in Table I.

TABLE I. The estimate of the first three central moments  $m_i$  of the FF and QE multiplicity distributions extracted from the measured fold distributions according to Ockels [52].  $p$  and  $r$  are the two parameters of a negative binomial distribution.  $\mu_3$  is the third moment computed using Eq. (3). (See text for more details.)

	$m_1$	$m_2$	$m_3$	$p$	$r$	$\mu_3$
FF	$12.5 \pm 0.4$	$23 \pm 6$	$100 \pm 240$	0.46	14.4	0.57
QE	$0.46 \pm 0.05$	$1.0 \pm 0.5$	$1.2 \pm 0.6$	0.54	0.39	3.34

The relationships of the central moments  $m_i$  with the shape parameters are the following:

$$\langle M \rangle = m_1, \sigma_M = \sqrt{m_2}, \tilde{m}_3 = \frac{m_3}{m_2^{3/2}}, \quad (1)$$

where  $\langle M \rangle$ ,  $\sigma_M$ , and  $\tilde{m}_3$  are the estimate of the average, standard deviation, and skewness of a candidate multiplicity distribution, respectively. The limited statistics obtained in the experiment do not allow us to determine the skewness and the kurtosis with good precision. For the QE channel, being the maximum measured fold of 2, only up to three moments could be extracted [52].

### A. From $\gamma$ -ray fold distribution to $M_r$ distribution in the FF and QF channels

We have tested several trial distributions, with fixed moments as in Table I, the best of which is, in both the FF and QE channels, the negative binomial defined as

$$f(k; r, p) = \binom{k+r-1}{k} (1-p)^r p^k \quad (2)$$

with shape parameters given by

$$\mu_1 = \frac{pr}{1-p}, \mu_2 = \frac{pr}{(1-p)^2}, \mu_3 = \frac{1+p}{\sqrt{pr}}. \quad (3)$$

By considering  $m_1$  and  $m_2$  from Table I as estimates of the shape parameters  $\mu_1$  and  $\mu_2$ , respectively, the distribution parameters  $p$  and  $q$  were calculated and are reported in Table I for QE and FF channels. Figure 10 shows the plot of the negative binomial distributions with parameters given in Table I. Min and Max in the legend correspond to the limiting distributions due to the errors in the moments. Figure 11 shows the obtained  $\gamma$ -fold distributions overlapped to the measured fold distributions.

We notice a very good agreement between the experimental and computed fold distributions in both channels. However, we have to remark that the negative binomial distribution has only two parameters,  $p$  and  $r$ . In other words,  $\mu_3$  is fully determined once  $p$  and  $r$  are fixed. Indeed, we could calculate, by Ockels' method, also an estimate of the third moment  $m_3$ . However,  $\mu_3$  as computed in Eq. (3), once  $p$  and  $r$  are fixed from the estimate of  $\langle M \rangle$  and  $\sigma_M$  alone, is not consistent with the one computed by Ockels' method ( $m_3$ ). This reflects the fact that the estimate of the third moment  $m_3$  is affected by an unreliable error given the low event statistics and the fact that Ockels' formula is limited to the case of an energy-independent efficiency.

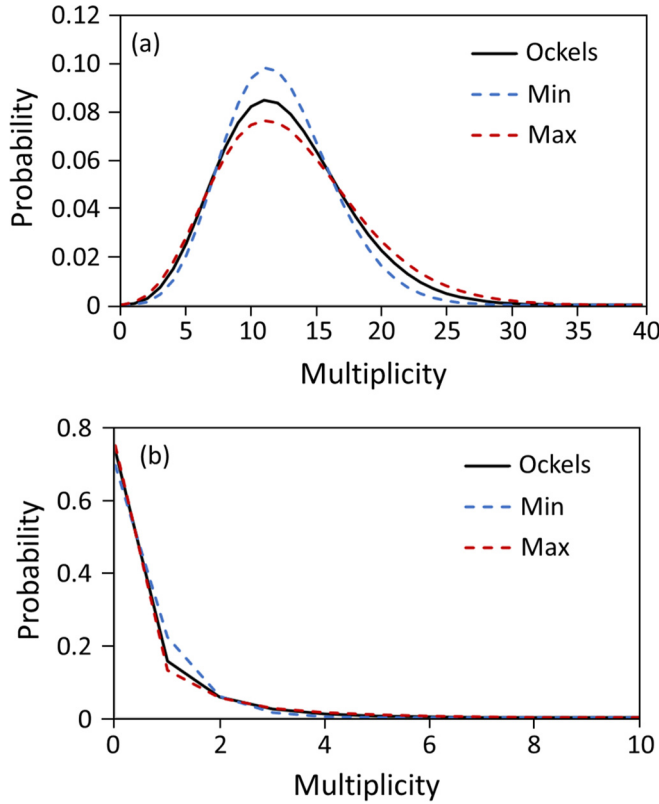


FIG. 10. Plot of the negative binomial distribution that reproduces at best the measured  $\gamma$ -fold distribution (a) for FF events and (b) for QE events. Min and Max in the legend correspond to the limiting distributions due to the errors in the shape parameters as in Table I.

### B. Comparison of the extracted $M_\gamma$ distribution in the FF channel with the calculation of the code GEF

To gain insight into the features of the FF events producing  $\gamma$ -ray distributions similar to the one shown in Fig. 10(a), GEneral description of Fission Observables (GEF) code [53] calculations have been carried out. All default GEF input parameters were kept, except for the root mean square angular momentum  $l_{\text{rms}}$  that was varied in order to better reproduce simultaneously the experimental FF mass-TKE distribution measured with CORSET and the coincident  $\gamma$ -ray energy spectra measured with ORGAM array. Then, the  $\gamma$ -ray multiplicity distribution corresponding to the GEF calculation, which better reproduces the FF channel observables, was filtered with SiMCA code, including the  $\gamma$ -ray response function of PARIS + ORGAM, to obtain the fold distribution. In Fig. 11(a), the experimental fold distribution in the FF channel is compared with the GEF prediction and the fold obtained assuming the negative binomial distribution with parameters determined with Ockels' method shown in Fig. 10(a).

In Fig. 12, the distributions of FF mass (a), TKE (b), and  $\gamma$ -ray energy (c) are compared with experimental data. The excellent agreement with these experimental observables could be reached for  $l_{\text{rms}} = 12.4\hbar$ . In Fig. 13, the corresponding GEF  $M_\gamma$  distribution is compared to the one with the parameters from Table I. Even this comparison shows an ex-

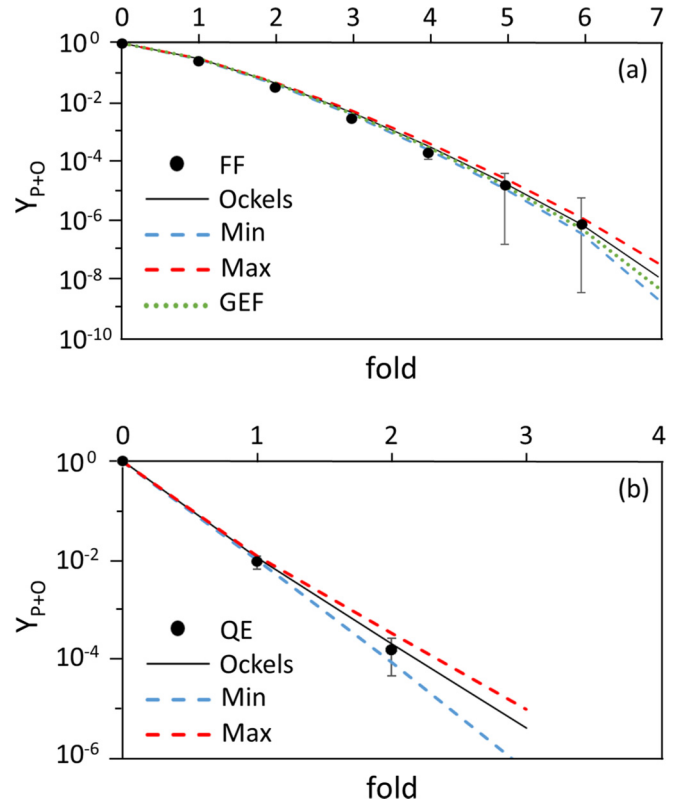


FIG. 11.  $\gamma$ -fold distributions in coincidence with FF (a) and QE (b) events compared to the respective fold distributions obtained after filtering the negative binomial distributions. In the case of FF events, the fold distribution obtained by the GEF code from the computed multiplicity distribution is also shown (see text). The curves labeled as Min and Max correspond to the limiting fold distributions due to the errors in the parameters as in Table I.

cellent agreement. Therefore, we can conclude that the whole procedure established to extract the experimental multiplicity distribution is substantially correct, even under the condition of a limited event statistics.

### VIII. FROM $M_\gamma$ DISTRIBUTION TO ANGULAR MOMENTUM TRANSFER IN FF AND QE CHANNELS

The final task of this data analysis is aimed at estimating, from the multiplicity distributions measured, the amount of channel orbital angular momentum  $|\vec{l}_i - \vec{l}_f|$  that is transformed into the angular momentum of the final fragments in the FF and QE channels.  $\vec{l}_i$  and  $\vec{l}_f$  are, respectively, the entrance and exit channel orbital angular momenta and are related, by the conservation law, to the spin of the two fragments at the scission point,  $\vec{J}_1$  and  $\vec{J}_2$ , namely,

$$\vec{l}_i = \vec{J}_1 + \vec{J}_2 + \vec{l}_f = \vec{J} + \vec{l}_f. \quad (4)$$

For the average values, we obtain

$$\langle J \rangle = \langle |\vec{l}_i - \vec{l}_f| \rangle. \quad (5)$$

In other words,  $\langle J \rangle$  is the average angular momentum transferred from the orbital angular momentum to the intrinsic spin

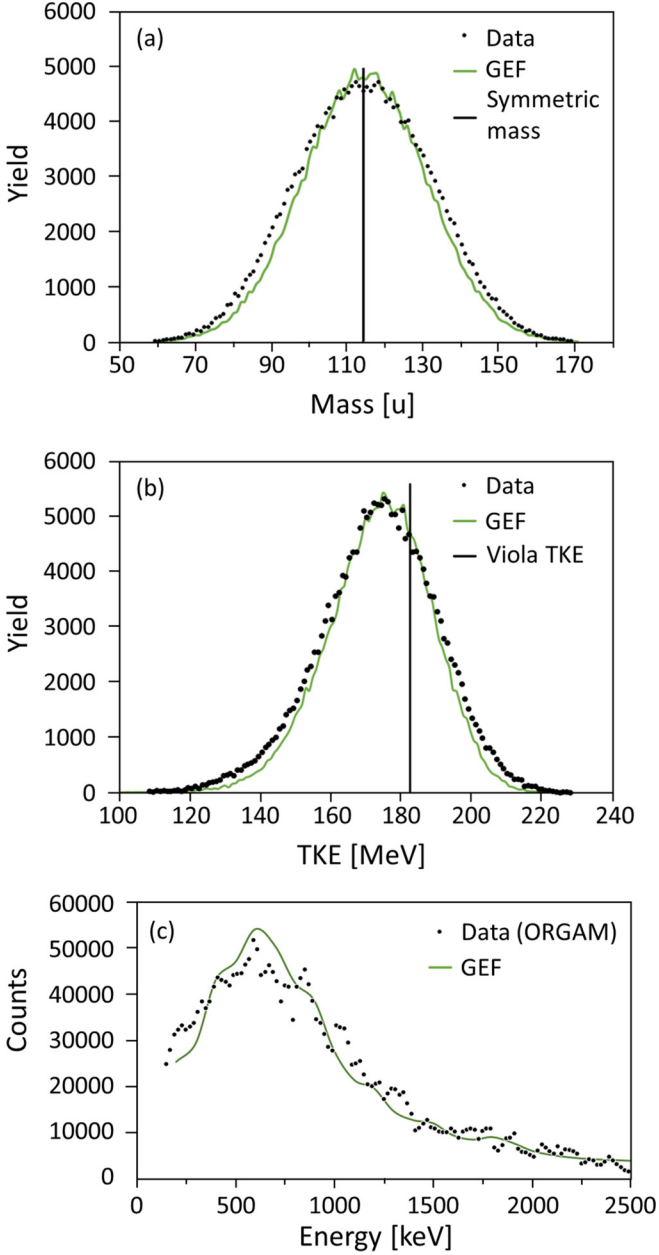


FIG. 12. Measured mass (a), TKE (b), and  $\gamma$ -ray energy spectra (from ORGAM only) (c) in the FF channel compared to GEF calculations for  $l_{\text{rms}} = 12.4\hbar$  and compound nucleus excitation energy  $E_{\text{CN}}^* = 43.5$  MeV.

of the fragments, the observable we are interested in this work.  $M_\gamma$  distributions include contributions from both fragments but is independent of the relative orientation of their respective angular momenta  $\vec{J}_1$  and  $\vec{J}_2$ . Therefore,  $\langle M_\gamma \rangle$  depends on the average angular momentum  $\langle J \rangle$  at scission point.

The conversion from  $\langle M_\gamma \rangle$  to  $\langle J \rangle$  involves, however, some uncertainties. It is generally assumed that the fragments deexcite in two steps: first, emission of light particles, that carry away some angular momentum, and after  $\gamma$ -ray emission when the excitation energy becomes low enough to hinder particle emission. At this second stage, most of the decays

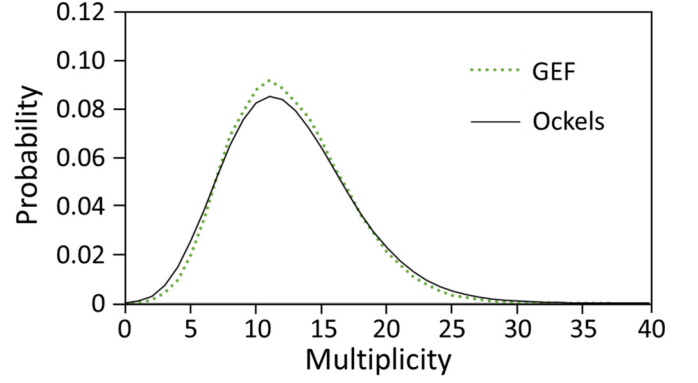


FIG. 13. Experimental  $M_\gamma$  distribution (Ockels' method) compared to the one obtained by using GEF with parameters fixed to reproduce the other measured observables (see text).

proceed via stretched  $E2$  transition, corresponding to a spin change equal to  $2\hbar$ , while a small number proceed via statistical  $\gamma$  ray by dipole transitions which correspond to an average spin change of  $0.5\hbar$ . The total amount of orbital angular momentum transferred into intrinsic angular momentum is hence given by

$$\langle J \rangle = \langle \Delta I_{lp} \rangle + \langle \Delta I_\gamma \rangle, \quad (6)$$

where  $\Delta I_{lp}$  and  $\Delta I_\gamma$  are the average angular momentum carried away by all light particles and all  $\gamma$  rays, respectively. Therefore, the measured  $\langle M_\gamma \rangle$  is a function of  $\langle J \rangle$  but also of the excitation energy at scission point.

Because of Eq. (6), the conversion  $\langle M_\gamma \rangle$  to  $\langle J \rangle$  suffers from the lack of knowledge of the spin removed by the evaporated particles and the average multiplicities of the  $\gamma$ -ray transitions. In the FF channel, at the low energy of our reaction, mostly neutrons are evaporated. From the data analysis performed in Ref. [36], an average of six neutrons are emitted per fission decay, in agreement with GEF predictions, and can carry away on average  $0.5\hbar$ . Therefore,  $\Delta I_{lp} = \langle N_n \rangle \langle l_n \rangle \simeq 3\hbar$ , where  $\langle N_n \rangle$  is the average number of evaporated neutrons and  $\langle l_n \rangle$  is the average angular momentum carried away by a single neutron.

Accordingly, for the  $\gamma$  rays we can take advantage of a common well-known expression [16,54]:

$$\Delta I_\gamma = 2(\langle M_\gamma \rangle - 2\alpha), \quad (7)$$

where  $\alpha$  is the average number of statistical (dipole) transitions. In this picture, stretched  $E2$  transitions take away most of the angular momentum. By reviewing the pertinent literature, we used the values of  $\alpha = 3$  as in Table II, which also shows the transferred angular momentum as computed from Eq. (6).

In the QE channel, the two nuclei barely overlap and their kinetic energies and masses are not altered appreciably [37,38]. Therefore, the nuclei, after a transfer of few nucleons, continue along Coulomb-like trajectories given the expected relatively low dissipation of energy and angular momentum. We do not expect the outgoing nuclei to carry enough excitation energy to induce neutron evaporation. Furthermore, only the very first few levels of the outgoing fragments can

TABLE II. Estimate of the orbital angular momentum transferred ( $J$ ) according to Eq. (6) in the QE and FF channels.  $\langle M_\gamma \rangle$  is the experimental average multiplicity and  $\alpha$ ,  $\langle l_n \rangle$ , and  $\langle N_n \rangle$  are the average number of statistical  $\gamma$ -ray (dipole) transitions, the average angular momentum carried away by a single neutron, and the average number of evaporated neutrons per fission events from fragments, respectively.

	$\langle M_\gamma \rangle$	$\alpha$	$\langle l_n \rangle$	$\langle N_n \rangle$	$\Delta I_{lp}$	$\Delta I_\gamma$	$\langle J \rangle$
FF	12.5	3	0.5	6	3	13	16
QE	0.5	0	0	0	0	0	1.5

be excited. Consequently, during the  $\gamma$  decay we can expect that on the average a  $\gamma$  ray can carry away  $1.5\hbar$  of angular momentum. Given the measured  $\langle M_\gamma \rangle \approx 0.5$  and  $\sigma_{M_\gamma} \approx 1$ , we reasonably deduce a narrow window of transferred angular momentum below  $3\hbar$  in the QE channel.

From Table II, it is quite evident a striking difference between the angular momentum transferred in the FF and QE channels that holds regardless of the assumptions underlying Eqs. (6) and (7). We could suspect about this strong contrast from the average  $\gamma$  multiplicities measured in the two channels, the implications of which will be discussed in the next section.

As a further support to the whole procedure used to measure  $M_\gamma$  and to connect it to the transferred angular momentum, we observe that our result is in noteworthy agreement with the systematics proposed by Ogihara *et al.* [55], which connects the average excitation energy of the fission fragments ( $E_f^*$ ) to the average angular momentum transferred to the fission fragments ( $J$ ) via the expression

$$\langle J \rangle = 0.11 \langle E_f^* \rangle / \text{MeV} + 7.5. \quad (8)$$

For  $\langle J \rangle = 16\hbar$ , Eq. (8) gives  $\langle E_f^* \rangle = 77$  MeV which is the maximum of the fission fragment excitation energy distribution derived in Ref. [36].

## IX. DISCUSSION

In the present measurements, the average  $\gamma$ -ray multiplicity  $\langle M_\gamma \rangle$  is used to determine the amount of angular momentum  $\langle J \rangle$  introduced into internal rotation of the fragments produced in two-body decays over the full range of impact parameters, from FF to QE reactions. It is found that in the FF channel,  $\langle J \rangle$  is much larger than in the QE channel. This result is understandable on the basis of the known picture of the FF and QE reaction paths. Classically, the conversion of orbital angular momentum of the entrance channel  $\vec{l}_i$  into intrinsic angular momentum of the fragments is described as the result of tangential friction. In a first step, the nuclei slide on each other and viscous forces set in a torque which puts them into rotation. For angular momenta close to the maximum, the two nuclei undergo grazing collisions. Since the two nuclei barely overlap, the kinetic energies and masses are not altered appreciably, and the nuclei continue along Coulomb-like trajectories. Hence, the reaction mechanism is confined to a very

narrow gap of orbital angular momentum around the grazing angle and only few nucleons are exchanged during a rather short interaction time.

For smaller impact parameters, or lower  $l$  waves, the closer contact leads to stronger damping of the kinetic energy and more extensive mass transfer. In these conditions, tangential forces continue to act until the system reaches a rolling stage in which the peripheral velocities are matched. The rolling friction slows down the rotation of the nuclei until they form a rigid body (sticking condition) [32,37]. According to this view of the angular momentum transfer, one expects a rapid increase of the angular momentum transferred to the fragments until the rolling state is reached with increasing interaction time. It can be demonstrated [37] that

$$J = \frac{2}{7} l_i. \quad (9)$$

For a further increase of the interaction time,  $J$  will continue to increase until it reaches its maximum value at the sticking point, where

$$J = \frac{I_1 + I_2}{I_1 + I_2 + I_{\text{rel}}} l_i \quad (10)$$

and where  $I_1$  and  $I_2$  are the moment of inertia of the fragments and  $I_{\text{rel}}$  is the moment of inertia of the relative motion. For smaller  $l$  waves, the system may fuse if the potential has a pocket [37]. The important point to remark here is that an increase of angular momentum transfer (or energy loss) is correlated to a growing interaction time. The maximum dissipation of angular momentum and energy correspond to complete fusion. The fused system may evolve as an evaporation residues or decays into fission. In any case, the complete fusion requires interaction times longer than peripheral reactions.

It is possible to check the consistency of the data in Table II with the above picture in mind. In the QE channel, the faster process,  $\langle J \rangle$  is only few units of  $\hbar$ , so almost no transfer of angular momentum occurs. Since this reaction is confined around the grazing angle  $l_{\text{gr}} = 25\hbar$ ,  $l_f$  remains confined around  $25\hbar$  and  $\text{TKE} \approx E_{\text{c.m.}}$ . In the FF channel (the slower process),  $l_i$  is fully transformed into intrinsic spin,  $\langle l_i \rangle \approx \langle J \rangle = 16\hbar$ . In the hypothesis of a triangular distribution,  $\langle l_i \rangle = 16\hbar$  corresponds to a maximum orbital momentum  $\langle l_{\text{max}} \rangle = 24\hbar$ . In other words, the whole ingoing orbital angular momentum distribution is exhausted by the FF and QE channels.

A further check on the outgoing orbital angular momentum  $l_f$  comes from the evaluation of the TKE. With the assumption of rigid rotation of the dinuclear complex at scission, the total kinetic energy of the fragments can be expressed as the sum of their Coulomb repulsion and rotational energies:

$$\text{TKE} = \frac{Z_1 Z_2 e^2}{d} + \frac{l_f(l_f + 1)\hbar^2}{2\mu d^2}, \quad (11)$$

where  $d$  is the separation distance of the fragments at scission and  $l_f$  is their relative orbital angular momentum. By taking the TKE at mass symmetry and considering the final fragment with ellipsoidal shape (with their axes of symmetry along the axis joining their center) having a deformation parameter  $\beta$

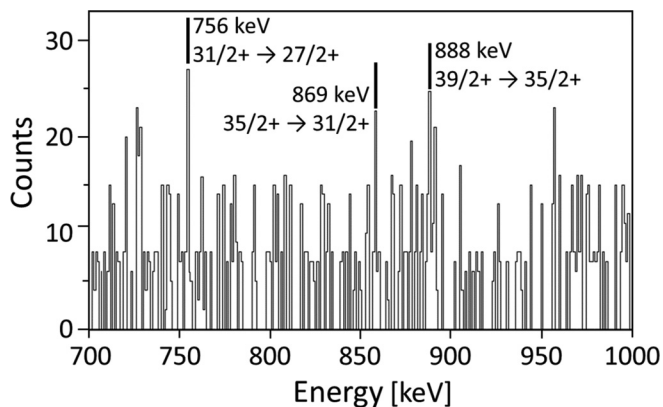


FIG. 14. High angular momentum transition  $\gamma$  rays of  $^{129}\text{La}$  in coincidence with fission fragments.

$= 0.6$ , we obtain  $l_f \approx 0$ . This result is in agreement with the hypothesis that the whole ingoing orbital angular momentum is dissipated and appears as spin of the fragments.

A further check in favor of the conclusion that higher  $\gamma$ -ray multiplicity is related to slower interaction time and higher angular momentum transfer comes from the spectroscopy of the discrete  $\gamma$  transitions in coincidence with FF and QE fragments. For this kind of analysis, corrections for Doppler effect are essential. The  $\gamma$ -ray energies have to be corrected for both fission fragments velocities, because it is impossible to know from which fragment the  $\gamma$  ray originates, and the two obtained Doppler corrected spectra have to be analyzed separately [56]. For instance, an entire set of  $\gamma$ -ray transitions have been found for the nucleus  $^{129}\text{La}$  connecting the level with  $E^* = 5934.2$  keV and  $J^\pi = 39/2^+$  to the level with  $E^* = 3420.6$  keV and  $J^\pi = 27/2^+$ . Figure 14 shows the  $\gamma$ -ray energy spectra detected with the ORGAM array, in coincidence with masses in the range  $(130 \pm 3$  amu) and one low-lying transition  $(270 \pm 5$  keV) of the  $^{129}\text{La}$  isotope ( $E_\gamma = 269.7$  keV), Doppler corrected for the  $^{129}\text{La}$  fragment. This result confirms the expectation that in the FF process higher angular momentum levels can be populated. We did not find the same result in the  $\gamma$  spectra in coincidence with QE fragments. Consequently, also the  $\gamma$ -spectroscopy analysis supports the idea that processes with longer timescales can convert much more orbital angular momentum into spin of the fragments. We can reasonably expect the same effect also in QF and FF.

As a final comment, we observe that  $^{129}\text{La}$  is a proton-rich nucleus, and thus the partner must be the neutron rich nucleus  $^{100}\text{Sr}$ , whose level scheme is only fairly known. This means that looking for more proton-rich nuclei (for instance, the partner of the well-known  $^{127}\text{La}$  is the unknown  $^{102}\text{Sr}$ ) with FF or QF reaction channels, it might be possible to populate unknown neutron-rich nuclei and the reconstruction of their level scheme can be pursued by using fragment-fragment coincidences. This is a very important indication for future experiments, to be performed with larger efficiency and event statistics, because there is no other known reaction mechanism to study such nuclei.

## X. CONCLUSIONS

$\gamma$ -ray multiplicity  $M_\gamma$  distributions were measured in the system  $^{32}\text{S} + ^{197}\text{Au}$  in coincidence with the QE and FF fragments. The aim is to show that by selecting faster and slower processes in the mass-TKE matrix, the slower process is characterized by a larger transfer of the ingoing orbital angular momentum. The interpretation of the data is supposed to rely on the fact that QE and FF reaction paths are known to be at the extreme of the interaction timescale: the fastest and the slowest, respectively. It is found that the average values of such  $M_\gamma$  distributions are consistent with a full transfer of the ingoing orbital angular momentum  $l_i$  to the spin of the fragments on the FF channel, whereas only a few units of  $\hbar$  are transferred to the QE fragments.

The observation that the average  $\gamma$ -ray multiplicity  $\langle M_\gamma \rangle$  is larger for the slower reaction channel gives support to the expectation that increasing amounts of orbital angular momentum can be transferred only by selecting increasingly slower processes. It is important to remark that the observed quantities are the lower moments of the multiplicity distribution (mean and variance). These quantities cannot therefore be obtained on an event-by-event basis, but only as an average over a sample of events. Consequently, those averages cannot be used for the reverse process of data analysis, namely, the selection of a slower process by gating on the multiplicity distribution. However, the most direct observable is the  $\gamma$ -fold distribution. Figure 6 is thus the key result of this work and shows that gating on higher fold processes favors the selection of the slower process. This result suggests that the  $\gamma$ -ray probe can play a very important role in disentangling FF and QF in the regions of the mass-TKE matrix where they are overlapped. The expectation is that QF is a process faster than FF and should give rise to a lower  $\gamma$  multiplicity, namely, smaller  $\gamma$ -fold values. To attain this separation, a large efficiency for  $\gamma$ -ray detection would be mandatory.

As a by-product of this analysis, we have found out that neutron-rich (possibly unknown) nuclei can be populated as partners of proton-rich nuclei. This means that completely new spectroscopy can be accessible by using fragment-fragment coincidences.

For future plans, it is crucial to test this method in condition of major interest: when FF and QF are overlapped with comparable intensity in the same mass region. However, an intermediate step would be to measure the  $\gamma$ -fold distribution in systems where QF is dominant. It would also be important to benefit of the properties of the QF to populate unknown neutron-rich nuclei. Reactions can be chosen carefully to populate neutron-rich regions of the nuclide chart of specific interest, like the one of interest from the r-process. However, it is evident that the experimental condition must be kept at the optimum and that much larger  $\gamma$ -ray detection efficiency and event statistics are necessary.

## ACKNOWLEDGMENTS

We would like to thank the IPNO accelerator group for the excellent beam quality and smooth running of the

experiment. The use of detectors from the Gammapool European Spectroscopy and France UK (IN2P3/STFC) Loan-Pool Resources through the ORGAM (Orsay Gamma Array) project is gratefully acknowledged. We also want to acknowledge the PARIS ongoing collaboration. This work was supported by Istituto Nazionale di Fisica Nucleare (INFN, Italy),

FLNR, JINR, the IN2P3-JINR Agreements No. 14-90 and No. 00-50, the ENSAR2 Project No. N-SI-88, the financial contribution of Romania to the Joint Institute of Nuclear Research (JINR-RO) to the 03-5-1094-2010/2016 and 03-5-1130-2017/2021 themes, the Polish National Science Centre under Contract No. 2013/08/M/ST2/00257.

- 
- [1] Y. T. Oganessian, A. Sobiczewski, and G. M. Ter-Akopian, *Phys. Scr.* **92**, 023003 (2017), and references therein.
- [2] S. Hofmann, S. Heinz, R. Mann, J. Maurer, G. Münzenberg, S. Antalic, W. Barth, H. G. Burkhard, L. Dahl, K. Eberhardt *et al.*, *Eur. Phys. J. A* **52**, 180 (2016).
- [3] R. C. Barber, H. W. Gaggeler, P. J. Karol, H. Nakahara, E. Vardaci, and E. Vogt, *Pure Appl. Chem.* **81**, 1331 (2009).
- [4] R. C. Barber, P. J. Karol, H. Nakahara, E. Vardaci, and E. W. Vogt, *Pure Appl. Chem.* **83**, 1485 (2011).
- [5] P. J. Karol, R. C. Barber, B. M. Sherril, E. Vardaci, and T. Yamazaki, *Pure Appl. Chem.* **88**, 139 (2016).
- [6] P. J. Karol, R. C. Barber, B. M. Sherril, E. Vardaci, and T. Yamazaki, *Pure Appl. Chem.* **88**, 155 (2016).
- [7] E. Vardaci, M. G. Itkis, I. M. Itkis, G. Knyazheva, and E. M. Kozulin, *J. Phys. G: Nucl. Part. Phys.* **46**, 103002 (2019).
- [8] E. Vardaci, A. Di Nitto, A. Brondi, G. La Rana, R. Moro, P. N. Nadtochy, M. Trotta, A. Ordine, A. Boiano, M. Cinausero *et al.*, *Eur. Phys. J. A* **43**, 127 (2010).
- [9] A. Di Nitto, E. Vardaci, A. Brondi, G. La Rana, R. Moro, P. N. Nadtochy, M. Trotta, A. Ordine, A. Boiano, M. Cinausero *et al.*, *Eur. Phys. J. A* **47**, 83 (2011).
- [10] E. Vardaci, P. N. Nadtochy, A. Di Nitto, A. Brondi, G. La Rana, R. Moro, P. K. Rath, M. Ashaduzzaman, E. M. Kozulin, G. N. Knyazheva *et al.*, *Phys. Rev. C* **92**, 034610 (2015).
- [11] E. Vardaci, A. Di Nitto, P. N. Nadtochy, and G. La Rana, *J. Phys. G: Nucl. Part. Phys.* **46**, 115111 (2019).
- [12] M. G. Itkis, E. Vardaci, I. M. Itkis, G. N. Knyazheva, and E. M. Kozulin, *Nucl. Phys. A* **944**, 204 (2015).
- [13] E. M. Kozulin, G. N. Knyazheva, S. N. Dmitriev, I. M. Itkis, M. G. Itkis, T. A. Loktev, K. V. Novikov, A. N. Baranov, W. H. Trzaska, E. Vardaci, S. Heinz, O. Beliuskina, S. V. Khlebnikov *et al.*, *Phys. Rev. C* **89**, 014614 (2014).
- [14] E. M. Kozulin, V. I. Zagrebaev, G. N. Knyazheva, I. M. Itkis, K. V. Novikov, M. G. Itkis, S. N. Dmitriev, I. M. Harca, A. E. Bondarchenko, A. V. Karpov, V. V. Saiko, and E. Vardaci, *Phys. Rev. C* **96**, 064621 (2017).
- [15] A. Di Nitto, J. Khuyagbaatar, D. Ackermann, L.-L. Andersson, E. Badura, M. Block, H. Brand, I. Conrad, D. M. Cox, Ch. E. Düllmann *et al.*, *Phys. Lett. B* **784**, 199 (2018).
- [16] R. Bock, Y. T. Chu, M. Dakowski, A. Gobbi, E. Grosse, A. Olmi, H. Sann, D. Schwalm, U. Lynen, W. Müller *et al.*, *Nucl. Phys. A* **388**, 334 (1982).
- [17] J. Töke, R. Bock, G. X. Dai, A. Gobbi, S. Gralla, K. D. Hildenbrand, J. Kuzminski, W. F. J. Müller, A. Olmi, H. Stelzer, B. B. Back, S. Bjørnholm *et al.*, *Nucl. Phys. A* **440**, 327 (1985).
- [18] W. Q. Shen, J. Albinski, A. Gobbi, S. Gralla, K. D. Hildenbrand, N. Herrmann, J. Kuzminski, W. F. J. Müller, H. Stelzer, J. Töke, B. B. Back, S. Bjørnholm, S. P. Srensen *et al.*, *Phys. Rev. C* **36**, 115 (1987).
- [19] R. Butsch, D. J. Hofman, C. P. Montoya, P. Paul, and M. Thoennessen, *Phys. Rev. C* **44**, 1515 (1991).
- [20] R. du Rietz, D. J. Hinde, M. Dasgupta, R. G. Thomas, L. R. Gasques, M. Evers, N. Lobanov, and A. Wakhle, *Phys. Rev. Lett.* **106**, 052701 (2011).
- [21] G. N. Knyazheva, I. M. Itkis, and E. M. Kozulin, *J. Phys.: Conf. Ser.* **515**, 012009 (2014).
- [22] A. Wakhle, C. Simenel, D. J. Hinde, M. Dasgupta, M. Evers, D. H. Luong, R. du Rietz, and E. Williams, *Phys. Rev. Lett.* **113**, 182502 (2014).
- [23] C. Simenel and A. S. Umar, *Prog. Part. Nucl. Phys.* **103**, 19 (2018).
- [24] D. Hilscher and H. Rossner, *Ann. Phys. (France)* **17**, 471 (1992), and references therein.
- [25] D. Jacquet and M. Morjean, *Prog. Part. Nucl. Phys.* **63**, 155 (2009), and references therein.
- [26] A. Gavron, A. Gayer, J. Boissevain, H. C. Britt, T. C. Awes, J. R. Beene, B. Cheynis, D. Drain, R. L. Ferguson, F. E. Obenshain *et al.*, *Phys. Rev. C* **35**, 579 (1987).
- [27] D. J. Hinde, H. Ogata, M. Tanaka, T. Shimoda, N. Takahashi, A. Shinohara, S. Wakamatsu, K. Katori, and H. Okamura, *Phys. Rev. C* **39**, 2268 (1989).
- [28] P. N. Nadtochy, E. Vardaci, A. Di Nitto, A. Brondi, G. La Rana, R. Moro, M. Cinausero, G. Prete, N. Gelli, and F. Lucarelli, *Phys. Lett. B* **685**, 258 (2010).
- [29] R. Moro, A. Brondi, N. Gelli, M. Barbui, A. Boiano, M. Cinausero, A. Di Nitto, D. Fabris, E. Fioretto, G. La Rana *et al.*, *Eur. Phys. J. A* **48**, 159 (2012).
- [30] A. Di Nitto, E. Vardaci, A. Brondi, G. La Rana, M. Cinausero, N. Gelli, R. Moro, P. N. Nadtochy, G. Prete, and A. Vanzanella, *Phys. Rev. C* **93**, 044602 (2016).
- [31] A. Di Nitto, E. Vardaci, G. La Rana, P. N. Nadtochy, G. Prete *et al.*, *Nucl. Phys. A* **971**, 21 (2018).
- [32] V. V. Volkov, *Phys. Rep.* **44**, 93 (1978).
- [33] B. B. Back, S. Bjørnholm, T. Døssing, W. Q. Shen, K. D. Hildenbrand, A. Gobbi, and S. P. Sørensen, *Phys. Rev. C* **41**, 1495 (1990).
- [34] H. Paşca, Sh. A. Kalandarov, G. G. Adamian, and N. V. Antonenko, *Phys. Rev. C* **96**, 044611 (2017).
- [35] B. B. Back, R. R. Betts, J. E. Gindler, B. D. Wilkins, S. Saini, M. B. Tsang, C. K. Gelbke, W. G. Lynch, M. A. McMahan, and P. A. Baisden, *Phys. Rev. C* **32**, 195 (1985).
- [36] E. M. Kozulin, I. M. Harca, E. Vardaci, I. Matea, A. Maj, I. Itkis, G. Knyazheva, K. Novikov, O. Dorvaux, M. Ciemala *et al.*, *Eur. Phys. J. A* **56**, 6 (2020).
- [37] R. Bass, *Nuclear Reactions with Heavy Ions* (Springer-Verlag, Berlin, 1980).
- [38] V. Zagrebaev, in *Heavy Ion Reactions at Low Energies*, Lecture Notes in Physics Vol. 963, edited by A. Denikin, A. Karpov, and N. Rowley (Springer Nature Cham, Switzerland, 2019).
- [39] M. G. Itkis and A. Y. Rusanov, *Phys. Part. Nuclei* **29**, 160 (1998).

- [40] V. E. Viola, K. Kwiatkowski, and M. Walker, *Phys. Rev. C* **31**, 1550 (1985).
- [41] E. M. Kozulin, A. A. Bogachev, M. G. Itkis, I. M. Itkis, G. N. Knyazheva, N. A. Kondratiev, L. Krupa, I. V. Pokrovsky, and E. V. Prokhorova, *Instrum. Exp. Tech.* **51**, 44 (2008).
- [42] P. J. Nolan, F. A. Beck, and D. B. Fossan, *Annu. Rev. Nucl. Part. Sci.* **44**, 561 (1994).
- [43] A. Maj, F. Azaiez, D. Jenkins, Ch. Schmitt, O. Stezowski, J. P. Wieleczko, D. Balabanski, P. Bednarczyk, S. Brambilla, F. Camera *et al.*, *Acta Phys. Pol. B* **40**, 565 (2009).
- [44] C. Boiano, S. Brambilla, S. Riboldi, A. Giaz, F. Camera *et al.*, in *IEEE Nuclear Science Symposium and Medical Imaging Conference (NSS/MIC), 2015, San Diego, CA* (IEEE, Piscataway, NJ, 2015), pp. 1–3.
- [45] M. Romoli, M. Di Pietro, E. Vardaci, A. De Francesco, M. Mazzocco, R. Bonetti, A. De Rosa, T. Glodariu, A. Guglielmetti, G. Inglima *et al.*, *IEEE Trans. Nucl. Sci.* **52**, 1860 (2005).
- [46] C. Signorini, D. Pierroutsakou, B. Martin, M. Mazzocco, T. Glodariu, R. Bonetti, A. Guglielmetti, M. La Commara, M. Romoli, M. Sandoli, E. Vardaci *et al.*, *Eur. Phys. J. A* **44**, 63 (2010).
- [47] D. Pierroutsakou, B. Martin, T. Glodariu, M. Mazzocco, R. Bonetti, A. De Francesco, A. De Rosa, F. Farinon, A. Guglielmetti, G. Inglima *et al.*, *Eur. Phys. J.: Spec. Top.* **150**, 47 (2007).
- [48] M. Mazzocco, C. Signorini, M. Romoli, R. Bonetti, A. De Francesco, A. De Rosa, M. Di Pietro, L. Fortunato, T. Glodariu, A. Guglielmetti *et al.*, *Eur. Phys. J.: Spec. Top.* **150**, 37 (2007).
- [49] N. Patronis, A. Pakou, D. Pierroutsakou, A. M. Sánchez-Benítez, L. Acosta, A. Boiano, G. Inglima, D. Filipescu, T. Glodariu, N. Alamanos *et al.*, *Phys. Rev. C* **85**, 024609 (2012).
- [50] E. M. Kozulin, E. Vardaci, G. N. Knyazheva, A. A. Bogachev, S. N. Dmitriev, I. M. Itkis, M. G. Itkis, A. G. Knyazev, T. A. Loktev, K. V. Novikov *et al.*, *Phys. Rev. C* **86**, 044611 (2012).
- [51] A. Maj, J. J. Gaardhøje, A. Ataç, S. Mitarai, J. Nyberg, A. Virtanen, A. Bracco, F. Camera, B. Million, M. Pignanelli *et al.*, *Nucl. Phys. A* **571**, 185 (1994).
- [52] W. J. Ockels, *Z. Phys. A* **286**, 181 (1978).
- [53] K.-H. Schmidt, B. Jurado, C. Amouroux, and C. Schmitt, *Nucl. Data Sheets* **131**, 107 (2016).
- [54] R. P. Schmitt, G. Mouchaty, and D. R. Haenni, *Nucl. Phys. A* **427**, 614 (1984).
- [55] M. Ogihara, H. Fujiwara, S.C. Jeong, W. Galster, S.M. Lee, Y. Nagashima, T. Mikumo, H. Ikezoe, K. Ideno, Y. Sugiyama, Y. Tomita *et al.*, *Z. Phys. A* **335**, 203 (1990).
- [56] E. M. Kozulin, E. Vardaci, I. M. Harca, C. Schmitt, I. Itkis, G. Knyazheva, K. Novikov, A. Bogachev, S. Dmitriev, T. Loktev *et al.*, *Eur. Phys. J. A* **52**, 293 (2016).